Time-of-flight based imaging in strong scattering underwater environments

Xin Jin,[*] ⓘ Dongyu Du, ⓘ Jiawei Jin, and Yihui Fan ⓘ

Shenzhen International Graduate School, Tsinghua University, Shenzhen 518055, China
[*]*jin.xin@sz.tsinghua.edu.cn*

Abstract: Time-of-flight (TOF) based underwater imaging is of great importance in practical applications due to its high image quality. Existing works separate scattered and ballistic photons in the time and space domains to recover objects in weakly scattered underwater scenes. However, in turbid underwater environments, absorption and strong anisotropic scattering cause weak ballistic light tightly coupled with forward-scattered and backward-scattered photons. The difficulty in isolating scattered light significantly limits the imaging capabilities of the existing methods. To tackle the problem, a forward-backward-distinctive imaging model is proposed, which models the spatial distribution of forward scattered illumination by point spread function (PSF) of the turbid water while modeling the backward scattered field by diffusion equation (DE) to describe the anisotropic scattering in the water accurately. Based on this, the underwater boundary migration model (WBMM) is derived, an explicit mapping relationship between the scene and the measurements is established, and a reconstruction algorithm utilizing time-of-flight information in the turbid water is realized. Experiments on a real scattering imaging system are conducted to demonstrate the effectiveness of the proposed method. Experimental results show that the proposed method outperforms the existing methods in terms of reconstruction accuracy and imaging limit subjectively and objectively. Even though the signal photons are highly scattered in turbid water, and the spatial distribution of the reflected light are greatly changed, the proposed method can reconstruct an object with a one-way scattering length of 9.5 mean transmission free-range (TMFPs), corresponding to a round-trip scattering length of 19 TMFPs, which is very favorable for dealing with underwater scattering imaging problems.

1. Introduction

Underwater optical imaging is gaining increasing attention in underwater archaeology, biological research, and engineering inspection due to its high resolution and high accuracy. However, optical imaging encounters substantial challenges owing to the strong absorption and scattering effects in turbid water. The strong absorption greatly reduces the energy of light that reaches and is reflected by the target. Scattering particles cause the illuminating light and the reflected light to be reflected and deflected multiple times along the propagation path, generating high-intensity scattering noise and thereby degrading the imaging quality. Meanwhile, turbid water exhibits pronounced anisotropic scattering properties [1], causing light to change direction multiple times at slight angles during propagation [2,3,4]. This leads to a drastic disruption of the original spatial light distribution, as even a highly collimated beam disperses into a diffuse light cloud as it propagates forward [4]. Therefore, addressing the imaging challenges posed by scattering in turbid water remains a critical and meaningful research endeavor.

According to the input data type, underwater scattering imaging techniques can be categorized into 2D image based methods and time-of-flight(TOF) based methods. The 2D image-based methods [5,6,7,8] achieve visual enhancement by correlating scattering with color channels. However, these methods are strictly limited by environmental factors, as stronger scattering and suboptimal lighting conditions can significantly degrade the quality of the enhanced images.

Therefore, to achieve underwater imaging in complex strong scattering environments, three-dimensional spatiotemporal measurements, including time-of-flight information, are introduced. In turbid water, the presence of strong forward- and backward-scattered photons creates significant imaging challenges. Existing TOF-based underwater imaging methods address these challenges by isolating scattered photons or extracting ballistic photons to reconstruct targets. At the hardware level, backward-scattered photons are isolated by setting reasonable time gating [9,10] and adjusting the relative positions of the illuminator and receiver [11], while forward-scattered photons are isolated by narrowing the field of view (FOV) of the detector [12,13,14]. At the algorithmic level, researchers employ techniques such as cross-correlation, spatial filtering, and statistical modeling to achieve scattering resistance. Pixel-wise cross-correlation [12,13,14,15,16] leverages the temporal-domain response of the detector as a prior, extracting ballistic light to compute the target's albedo and depth. Spatial filtering methods smooth the intensity map of the measurements using techniques like median filtering [15] and mode filtering [17], attenuating noise stemming from forward and backward scattering. Statistical modeling methods [10,18,19] formulate maximum likelihood problems in the temporal domain or across multiple pixels to address the sparsity of ballistic light caused by scattering. All these methods that separate ballistic light from scattered light can mitigate interference from scattering noise and enhance signal-to-noise ratio. However, in the turbid water with strong scattering, ballistic photons are extremely attenuated and easily overwhelmed by scattered photons. As a result, ballistic and scattered photons don't have distinguishable characteristics in both temporal and spatial domains, leading to the failure of these methods. Additionally, incorporating polarization states into TOF measurements [9,20,21] can achieve ballistic light separation, but this addition, while providing more information, significantly increases the complexity of measurements and algorithms.

Notably, imaging methods that employ scattering propagation modeling demonstrate superior performance in strong scattering environments. Lindell [22] demonstrated a three-stage propagation model for scattering imaging, which includes two segments of transmission through the scattering medium and one segment of free-space propagation, enabling clear reconstruction of objects behind a thick scattering layer. Du [23,24] employed the diffusion equation to model photon propagation in a volume-scattering medium and reconstructed objects encased in foam by solving an inverse problem with an attenuation limit of 24 TMFPs. However, these methods rely on ideal isotropic media models, which cannot accurately depict the propagation dynamics of strong anisotropic scattering in turbid water, nor effectively handle the intense forward scattered light produced by such conditions.

To address this problem, in this paper, we propose a time-of-flight-based method for underwater scattering imaging. Unlike existing underwater scattering imaging methods, the proposed method models the underwater scattering propagation process. In this case, a forward-backward-distinctive imaging model is proposed, which uses the point spread function to model the spatial distribution of forward-scattered illumination in turbid water and the diffusion equation to accurately describe the anisotropic scattering of the backward-scattered field. To mitigate scattering effects in turbid water, the underwater boundary migration model is derived to establish an explicit mapping relationship between the scene and the measurements, thereby enabling the development of a reconstruction algorithm that utilizes time-of-flight information by solving the inverse problem. Experiments on a real scattering imaging system are conducted to demonstrate the effectiveness of the proposed method. The experimental results show that the proposed method outperforms existing methods in both subjective quality assessment and objective evaluation metrics, including peak signal-to-noise ratio (PSNR) and structural similarity index (SSIM). Using our imaging system, the proposed method can reconstruct object with a one-way scattering length of 9.5 TMFPs, corresponding to a round-trip scattering length of 19 TMFPs.

2.   Method

The method proposed in this paper is based on the confocal volumetric scattering imaging system, as depicted in Fig. 1. This system utilizes a pulsed laser for illumination, as shown in Fig. 1(a), and an ultrafast detector for detection, as shown in Fig. 1(b). Both the laser and detector share the same optical path, facilitated by a beam splitter that separates the light paths. The system scans the underwater scene pixel by pixel, capturing the time-domain response of each pixel with the detector to form a 3D spatio-temporal measurement containing time-of-flight information.
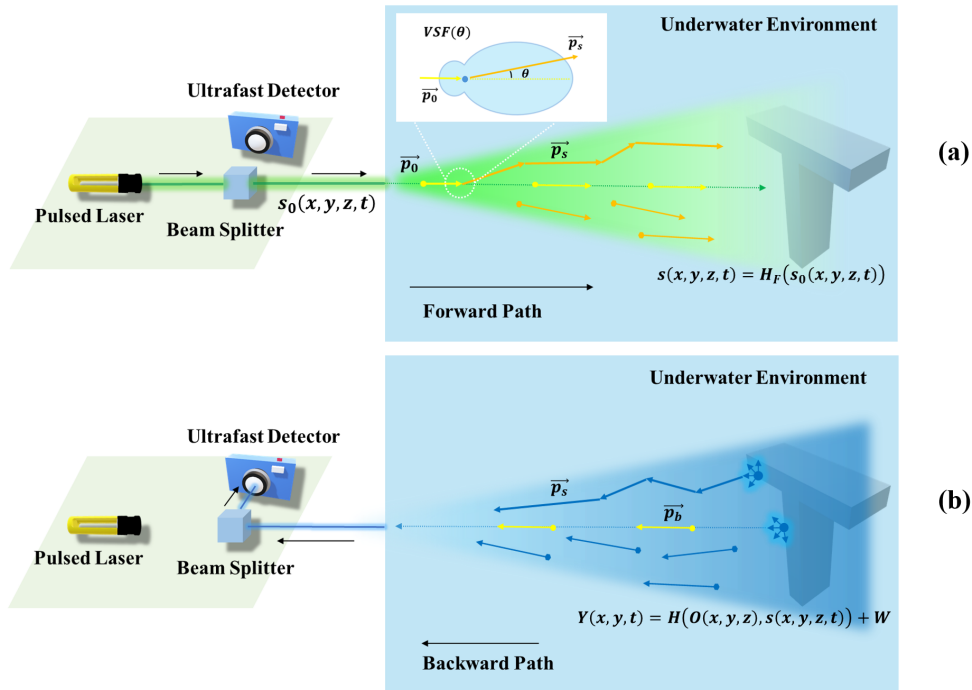

Fig. 1. Schematic diagram for Underwater TOF-based imaging. (a)The forward path in the imaging process. (b)The backward path in the imaging process.

   To reconstruct objects in turbid water, we propose a forward-backward-distinctive imaging model that accurately models the imaging process, as detailed in Section 2.1. Next, a boundary migration model for the scattering imaging process is derived, providing an analytical mapping relationship between the scene and the measurements, as described in Section 2.2. Finally, the target is reconstructed by solving the inverse problem of the boundary migration model, as detailed in Section 2.3.

2.1.   Underwater forward-backward-distinctive imaging model

The complete imaging process can be divided into two parts, the forward path shown in Fig. 1(a) and the backward path shown in Fig. 1(b). As shown in Fig. 1(a), a pulsed laser emits high-energy photons $\vec{p}_0$ to illuminate the scene. These photons travel into the underwater environment along a fixed direction, where they interact with the turbid water and form scattered photons $\vec{p}_s$. During each scattering event, the photons change their propagation direction, with the scattering angle θ obeying the volume scattering function $VSF(\theta)$. Due to the high anisotropic scattering properties of turbid water, the scattering angle θ is usually very small, causing multiple small-angle scatterings and forward propagation in various directions. These changes in the

propagation direction of scattered photons manifest macroscopically as changes in the intensity distribution of the illuminated light field $s(x, y, z, t)$, which can be modeled as:

$$s(x, y, z, t) = H_F(s_0(x, y, z, t)), \tag{1}$$

where $s_0(x, y, z, t)$ represents the illumination light field distribution in free space, dependent solely on the intrinsic parameters of the illuminator. The function $H_F(\cdot)$ denotes the transfer function for forward illumination propagation in turbid water. Assuming the scattering characteristics of turbid water remain constant over time and exhibit spatial translation invariance, $H_F(\cdot)$ can be modeled as the point diffusion function $P_w(x, y, z)$ of the turbid water. Thus, the transfer function $H_F(\cdot)$ can be expressed as the spatial convolution given as:

$$s(x, y, z, t) = H_F(s_0(x, y, z, t)) = p_w(x, y, z) * s_0(x, y, z, t), \tag{2}$$

where $*$ is the convolution operator applied per frame.

Significant research has focused on mathematically expressing the point diffusion function of turbid water [25,26]. A notable contribution is the small-angle approximation theory proposed by Wells [27], which assumes that single scattering in turbid water occurs at very small angles (less than 0.1 degrees). Using this assumption, simplified RTE equations solve the frequency-domain transfer function in turbid water. Based on Wells' theory, Hou [28] introduced an approximate form of the point diffusion function, providing high accuracy and a more explicit mathematical expression, given as follows:

$$p_w(x, y, z) = K(\theta_0)\frac{\omega\mu_c l(x, y, z)e^{-\mu_c l(x, y, z)}}{2\pi\theta(x, y, z)^{(1-2\mu_c l(x, y, z)\theta_0\omega)/\omega}}, \tag{3}$$

where, $K(\theta_0)$ is a constant related to the mean scattering angle θ_0, ω is the single scattering albedo of the turbid water, and $\mu_c = \mu_a + (1 - g)\mu_s$ denotes the total attenuation coefficient. The distance $l(x, y, z)$ and the scattering angle $\theta(x, y, z)$ at position (x, y, z) relative to the reference position (x_0, y_0, z_0). The backward path depicted in Fig. 1(b) includes the interaction between the forward light field and the scene, the reflected light then undergoes backward propagation and is captured by the ultrafast detector. The TOF measurements recorded by the ultrafast detector include both ballistic photons $\vec{p_b}$, which travel without scattering, and scattered photons $\vec{p_s}$ that have undergone multiple scattering events. These measurements can be modeled as:

$$Y(x, y, t) = H(O(x, y, z), s(x, y, z, t)) + W, \tag{4}$$

where, $Y(x, y, t)$ denotes the received time-of-flight measurement, $O(x, y, z)$ represents the bidirectional scattering distribution function (BRDF) of the objects in the scene, and $H(\cdot)$ represents the backward scattering transfer function of the turbid water, which characterizes the relationship between scene, illumination, and measurement. Additionally, W denotes additive random measurement noise. Due to the complexity of the scene and scattering propagation process, providing an explicit expression for the transfer function $H(\cdot)$ is often challenging. Therefore, the time-resolved diffusion equation is employed to implicitly characterize the anisotropic scattering propagation of the backward path, given as:

$$\frac{1}{c}\frac{\partial\phi(x, y, z, t)}{\partial t} - \nabla[D(x, y, z)\nabla\phi(x, y, z, t)] + \mu_a(x, y, z)\phi(x, y, z, t)$$
$$= s(x, y, z, t) = p_w(x, y, z) * s_0(x, y, z, t), \tag{5}$$

where $\phi(x, y, z, t)$ denotes the backward scattering field, c is the speed of light, and $D(x, y, z) = (3(\mu_a + (1 - g)\mu_s))^{-1}$ represents the diffusion coefficient, with μ_a as the absorption coefficient, μ_s

as the scattering coefficient, and g as the mean cosine of the scattering angle. Here, we assume that the scattering media is homogeneous, thus D is a constant.

For the backward scattering field, the object is treated as self-emissive, meaning the object emits a wave at $t = 0$. Then, the spatial intensity distribution of the self-emissive scene, denoted as $I(x, y, z)$, can be described by the temporal boundary of the backward scattering field, denoted as $\phi(x, y, z, t = 0)$. Given that the self-emissive field is primarily governed by the object, we have $I(x, y, z) \propto O(x, y, z)$. Furthermore, we set the scanning surface at $z = 0$, allowing the measurement $Y(x, y, t)$ to be represented by the spatial boundary of the backward scattering field, i.e., $\phi(x, y, z = 0, t)$. Under these conditions, the boundary conditions of the backward scattering field can be expressed as follows:

$$\begin{cases} \phi(x, y, z = 0, t) = Y(x, y, t) \\ \phi(x, y, z, t = 0) = I(x, y, z) \end{cases}, \tag{6}$$

By combining Eqs. (5) and (6), a comprehensive model for imaging in turbid water is established.

2.2. Underwater time-space boundary migration model

To solve the inverse problem of the forward-backward-distinctive imaging model described in Section 2.1, it is essential to derive the analytical mapping relation from the temporal boundary $\phi(x, y, z, t = 0)$ to the spatial boundary $\phi(x, y, z = 0, t)$ as follows:

$$\phi(x, y, z = 0, t) = H(\phi(x, y, z, t = 0)), \tag{7}$$

To obtain the implicit function $H(\cdot)$ represented by Eq. (5), we first perform a spatial Fourier transform $(x, y, z, t) \rightarrow (k_x, k_y, k_z, t)$ on the Eq. (5), which yields a first-order linear differential equation:

$$\frac{1}{c} \frac{\partial \Phi(k_x, k_y, k_z, t)}{\partial t} + \left[D \left(k_x^2 + k_y^2 + k_z^2 \right) + \mu_a \right] \Phi(k_x, k_y, k_z, t) \tag{8}$$
$$= P_w(k_x, k_y, k_z) \cdot S_0(k_x, k_y, k_z, t).$$

Solving this equation yields the general solution of $\Phi(k_x, k_y, k_z, t)$, which has the following form:

$$\Phi(k_x, k_y, k_z, t) = e^{-c\left[D\left(k_x^2 + k_y^2 + k_z^2\right) + \mu_a\right]t} \cdot \left[C(k_x, k_y, k_z) + \right.$$
$$\left. \int cP_w(k_x, k_y, k_z)S_0(k_x, k_y, k_z, t)e^{c\left[D\left(k_x^2 + k_y^2 + k_z^2\right) + \mu_a\right]t}dt \right]. \tag{9}$$

$C(k_x, k_y, k_z)$ is an arbitrary function introduced by the homogeneous solution of Eq. (8). $\Phi(k_x, k_y, k_z, t), P_w(k_x, k_y, k_z)$ and $S_0(k_x, k_y, k_z, t)$ represent the Fourier transform of $\phi(x, y, z, t)$, $p_w(x, y, z)$ and $s_0(x, y, z, t)$, respectively. Since $P_w(k_x, k_y, k_y)$ is independent of time, Eq. (9) can be further reorganized as follows:

$$\Phi(k_x, k_y, k_z, t) = e^{-c[D(k_x^2 + k_y^2 + k_z^2) + \mu_a]t} \cdot P_w(k_x, k_y, k_z)$$
$$\cdot \underbrace{\left[C(k_x, k_y, k_z) + \int cS_0(k_x, k_y, k_z, t)e^{c[D(k_x^2 + k_y^2 + k_z^2) + \mu_a]t}dt \right]}_{\Phi'(k_x, k_y, k_z)}, \tag{10}$$

where $\Phi'(k_x, k_y, k_z)$ is the spectrum of the temporal boundary $\phi(x, y, z, t = 0)$. To obtain the spatial boundary, we perform the inverse Fourier transform on Eq. (10) and using the dispersion

relation $f = c\sqrt{k_x^2 + k_y^2 + k_z^2}$ to map $\Phi'(k_x, k_y, k_z)$ to $\bar{\Phi}(k_x, k_y, f)$, which is the same as the existing methods [29,23]. After setting $z = 0$, the transformation from the temporal boundary to the spatial boundary can be analytically expressed as:

$$\phi(x, y, z = 0, t) = H(\phi(x, y, z, t = 0))$$

$$= p_w(x, y, z = 0) * F_{xy}^{-1}\{\frac{1}{2\pi} \int G_{k_z \to f}[F_{xyz}(\phi(x, y, z, t = 0))] \cdot e^{-\left(D\frac{f^2}{c} + c\mu_a\right)t} df\}, \quad (11)$$

where $F_{xy}^{-1}(\cdot)$ and $F_{xyz}(\cdot)$ represent the two-dimensional Fourier inverse transform and the three-dimensional Fourier transform, respectively, and $G_{k_z \to f}[\cdot]$ denotes the frequency-domain mapping relation for $(k_x, k_y, k_z) \to (k_x, k_y, f)$.

2.3. Underwater boundary migration algorithm

As depicted in Fig. 2(a), the model for underwater boundary migration comprises five distinct steps. To achieve target reconstruction in turbid water, the inverse of these steps need to be sequentially implemented, illustrated in Fig. 2(b). The reconstruction algorithm involves sequential divisions into frame-wise deconvolution, two-dimensional Fourier transform, inverse of numerical integration, frequency domain interpolation, and three-dimensional inverse Fourier transform. Firstly, for each time frame $\phi(x, y, 0, t = t_1)$, a deconvolution operation is performed using the 2D convolution kernel ψ from Eq. (3). In this process, the distance $l(x, y, z)$ and spatial scattering angle $\theta(x, y, z)$ are computed for each time frame based on the depth prior $z_1 = c' \cdot t_1$. Based on this, the 2D spatial deconvolution for each time frame is solved using Wiener filtering:

$$\phi'(x, y, z = 0, t = t_1) = F^{-1}\left(\frac{|F(\psi)|^2}{|F(\psi)|^2 + 1/\alpha} \cdot \frac{F(\phi(x, y, z = 0, t = t_1))}{F(\psi)}\right), \quad (12)$$

where $F(\cdot)$ and $F^{-1}(\cdot)$ denote the Fourier transform and its inverse, respectively. α is a parameter depended on the signal-to-noise ratio. To get $\bar{\Phi}(k_x, k_y, f)$, we first perform a Fourier transform of $\phi'(x, y, z = 0, t)$ in the spatial domain $(x, y) \to (k_x, k_y)$. Then, following the integration in Eq. (11), the transformation from t to f can be achieved. Specifically, this numerical transform process can be discretized as $\bar{\Phi}(f) = H_i^{-1} \cdot \phi'(t)$, where H_i^{-1} is the inverse matrix of the temporal transfer matrix H_i and has the following form:

$$H_i^{-1} = \begin{bmatrix} e^{-\left(D\frac{f_1^2}{c} + c\mu_a\right)t_1} & \cdots & e^{-\left(D\frac{f_M^2}{c} + c\mu_a\right)t_1} \\ \vdots & \ddots & \vdots \\ e^{-\left(D\frac{f_1^2}{c} + c\mu_a\right)t_M} & \cdots & e^{-\left(D\frac{f_M^2}{c} + c\mu_a\right)t_M} \end{bmatrix}_{M \times M}^{-1}. \quad (13)$$

M is the number of time bins. In our experiments, the condition number of H_i is very large, resulting in an ill-conditioned inverse problem. Therefore, we calculate the pseudo-inverse matrix of H_i to complete this numerical transformation process. Next, the conversion from the (k_x, k_y, f) domain to the (k_x, k_y, k_z) domain is achieved through frequency domain interpolation, as follows:

$$\Phi'(k_x, k_y, k_z) = \frac{c|k_z|}{\sqrt{k_x^2 + k_y^2 + k_z^2}} \bar{\Phi}\left(x, y, c\sqrt{k_x^2 + k_y^2 + k_z^2}\right). \quad (14)$$

Finally, the temporal boundary is derived through the inverse Fourier transform $(k_x, k_y, k_z) \to (x, y, z)$, given as:

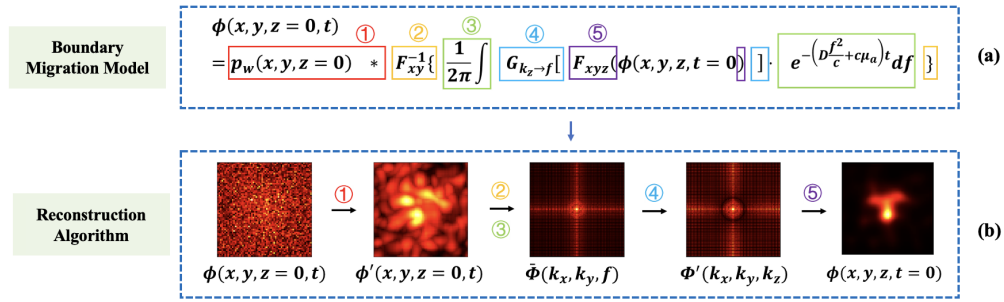$$\phi(x, y, z, t = 0) = F_{xyz}^{-1}(\Phi'(k_x, k_y, k_z)). \quad (15)$$

Fig. 2. The Flow Chart for the Underwater Boundary Migration Algorithm. (a)The flow chart for the underwater boundary migration model. (b)The flow chart for the reconstruction algorithm.

3. Experimental results and discussions

3.1. Experimental setup

To validate the effectiveness of the proposed method, we designed the experimental setup shown in Fig. 3(a) and utilized a scanning confocal volumetric scattering imaging system depicted in Fig. 3(b). In Fig. 3(a), a $0.5m \times 0.5m$ water tank simulated a turbid underwater environment, where the target object was fully immersed with Maalox as the scattering medium. The imaging system, as illustrated in Fig. 3(b), captured time-of-flight information in this turbid environment. The imaging system employed a high-power pulsed laser (INNO AMT-532-1W1M) operating at a wavelength of 532 nm with a pulse width of 12ps, a repetition frequency of 20 MHz, and an average optical power of 700 mW. After passing through a beam splitter (Thorlabs PBS251), the laser light was directed onto the scene by a galvanometer (Thorlabs GVS012) for pixel-wise scanning, controlled by a NI-DAQ USB-6343 data acquisition device. The reflected light followed the same path, passing through a galvanometer and beam splitter before being focused by a lens (focal length 2.8-12 mm, maximum f-value 1.6) onto a SPAD array (Photon Force PF32), acting as an ultrafast detector. Each pixel of the SPAD array operated in time-correlated single-photon counting (TCSPC) mode with a temporal resolution of 55ps. A time-delay unit (Micro Photon Devices PSD-065-A-MOD) shaped the laser's synchronization signal into a standard TTL trigger signal for acquisition by the SPAD array. This setup enabled three-dimensional temporal-spatial measurements, comprising two-dimensional spatial information (64×64) and one-dimensional temporal information (250 time bins) derived from measurements at all scanning points.

3.2. Experimental results

As shown in Fig. 3(a), Maalox suspensions is used to simulate the turbid water. Previous studies have shown that Maalox suspensions exhibit a volume scattering function similar to natural water, with strong scattering and little absorption [4]. To simulate a highly scattering underwater environment, we prepared Maalox suspensions at a concentration of 0.072%. Using Beer-Lambert's law, the attenuation coefficient is determined to be $\mu_c = 14.72m^{-1}$, giving an average free transmission range of $l^* = 1/\mu_c = 0.068m$. This implies that the photon's energy is attenuated by $1/e$ on average for every distance l^* traveled. Based on this, the attenuation length over a distance r can be calculated as $l_c = r/l^*$. The targets used include flat foam letters "T", "H", and "C" with Lambertian surfaces, combinations of letters at different depths "TL" and "VT", and three-dimensional mannequin with Lambertian surfaces. All targets were fixed with matte black supports and immersed in a water tank. The imaging system conducts a 64×64 pixel-wise scan over a $0.5m \times 0.5m$ area. Prior to each experiment, the scanning range is adjusted according to the objects' depths to ensure comprehensive coverage and photon information to be captured. The
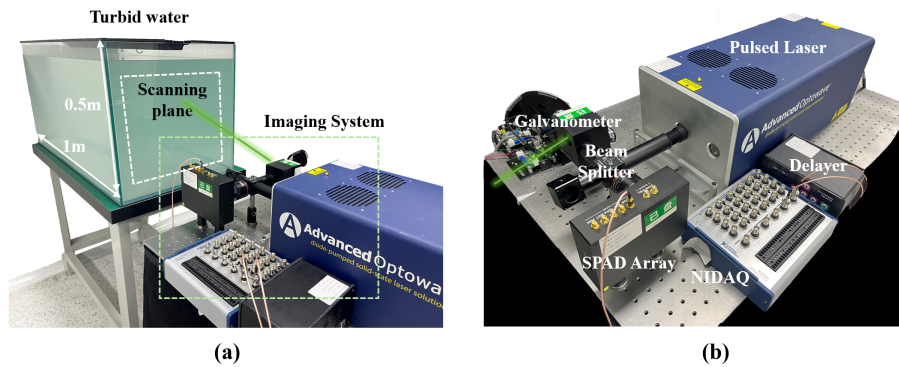
Fig. 3. The experimental and the imaging system setup. (a)The experimental setup. (b)The setup of the scanning confocal volume scattering system.

obtained measurement data were processed using time gating, pixel-wise cross-correlation [12], BMM [23], and the algorithm proposed in this paper. The reference image was acquired using the same imaging system without the scattering medium and then binarized. Reconstruction results were evaluated both subjectively and with objective metrics including PSNR and SSIM.

The proposed algorithm uses 3D TOF measurement data as input and follows the process outlined in Fig. 2(b). This includes frame-wise deconvolution, 2D Fourier transform, numerical integration inverse, frequency domain interpolation, and 3D Fourier inverse transform, with each step's results provided. Notably, while spatial domain frame-wise deconvolution can improve object visibility, it fails to reconstruct the object's shape effectively. This is because the PSF convolution model only accounts for the spatial distribution changes of the illumination light field during forward propagation, which is just one part of the complete imaging model. Reconstructing the object accurately requires solving the inverse problem of the entire imaging model.

Figure 4. shows the reconstruction results for various planar and three-dimensional target objects using time-gating, cross-correlation, BMM, and the proposed method. The time-gating method fails to distinguish the target objects, showing only slight bright spots. This is because ballistic photons in turbid water experience strong scattering and absorption, reducing their ratio and blending them with background noise from backscattering, making it difficult to extract ballistic photons from the time dimension alone. Pixel-wise cross-correlation improves contrast by using the system's time-domain response as a priori, but in strong scattering environments, the target is still only represented as a brighter region, making shape recognition difficult due to the sparsity of ballistic photons. The BMM algorithm, which models the propagation process using the diffusion equation, achieves significantly higher contrast than time-gating and cross-correlation. However, due to strong anisotropic scattering in water, forward-scattered photons and ballistic photons are highly coupled in the time domain. Time-gating and cross-correlation methods do not model scattering propagation, and the BMM algorithm does not account for forward propagation scattering. Consequently, these methods often reconstruct forward-scattered light artifacts as part of the object, resulting in blurred spatial morphology. In contrast, the proposed algorithm comprehensively models both stages of the illumination-imaging process in turbid water, effectively reconstructing objects with clear shapes and separating them from background noise, outperforming the other methods significantly.

To objectively evaluate the effectiveness of the proposed method, we calculated the PSNR and SSIM of all reconstruction results, as shown in Tables 1 and 2. The proposed method outperforms the others in both metrics. Time-gating and cross-correlation are ineffective when ballistic and
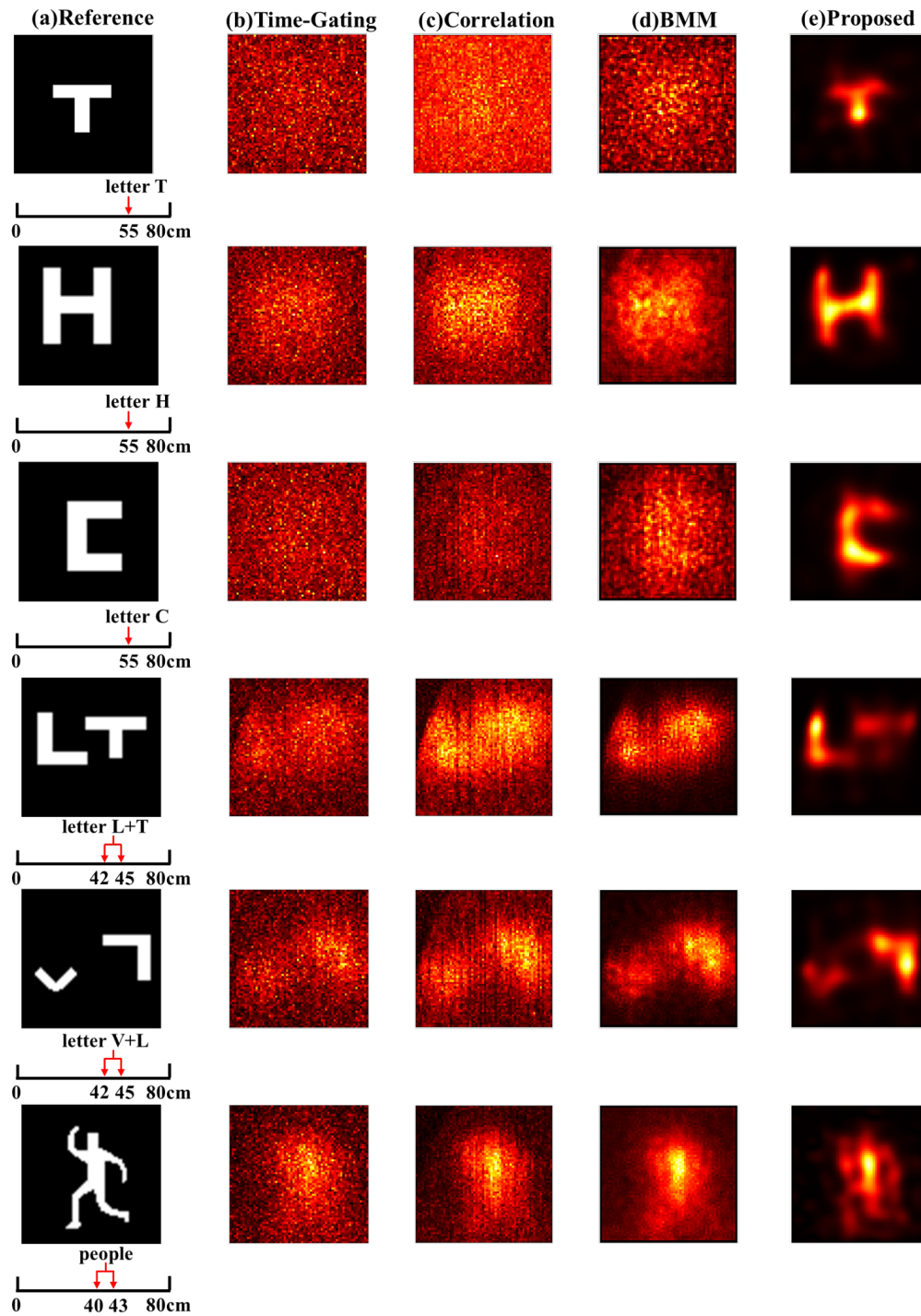
Fig. 4. Reconstruction results for different objects

scattered light are highly coupled, while the BMM algorithm improves contrast but still suffers from forward scattering noise, resulting in low PSNR of both these three methods. The proposed algorithm models the scattering propagation process in turbid water, effectively removing both forward and backward scattering noise, and achieving the highest PSNR in all experiments. Additionally, time-gating, cross-correlation, and BMM do not model forward propagation, leading to blurring from forward scattering and poor shape and structure discrimination of the target object. The proposed algorithm eliminates this scattering noise, reconstructing clear target objects with significantly higher structural similarity compared to other methods.

By varying the depth of the letter T from the measurement plane, we collected TOF measurements at different TMFPs. Figure 5. shows the temporal response of a single scanning point at different TMFPs. The system's temporal response includes a peak from the object's reflection containing both forward-scattered and ballistic photons, along with scattering noise from backward scattering. As TMFPs increase, the absorption attenuation and forward scattering in the turbid water also increase, resulting in a gradual decrease in the energy of photons from the object and a broadening in the time domain. This results in both the energy intensities and temporal distribution of signal photons and backscattered noise converging, posing a significant challenge for imaging due to heightened coupling between scattered and ballistic photons.
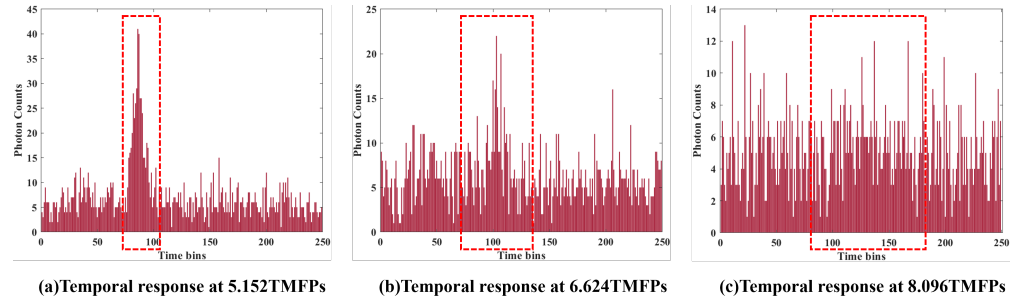

(a)Temporal response at 5.152TMFPs   (b)Temporal response at 6.624TMFPs   (c)Temporal response at 8.096TMFPs

Fig. 5. Comparison of Temporal Response under Different TMFPs

Table 1. Comparison in PSNR(dB) of Different Methods

Method	T	H	C	LT	VL	People	Average
Time-gating	5.9209	5.6973	6.0563	5.8837	6.1409	6.1599	5.9765
Correlation	7.4990	7.9969	9.1343	9.1884	9.6846	9.9899	8.9155
BMM	8.5790	9.0666	9.1770	10.8271	11.3250	11.0110	9.9976
Proposed	**12.5761**	**12.7456**	**13.3537**	**12.1662**	**13.6085**	**12.8884**	**12.8897**

Table 2. Comparison in SSIM of Different Methods

Method	T	H	C	LT	VL	People	Average
Time-gating	0.0812	0.1739	0.1090	0.1735	0.1211	0.2500	0.1514
Correlation	0.0478	0.2038	0.1297	0.1304	0.0867	0.3059	0.1507
BMM	0.1437	0.3191	0.2298	0.3603	0.3382	0.3556	0.2911
Proposed	**0.5574**	**0.7015**	**0.6967**	**0.5208**	**0.5033**	**0.5255**	**0.5842**

On this basis, we reconstructed the target object under different TMFPs using different methods, and the reconstruction results are shown in Fig. 6. It can be seen that the number of reflected photons from the object is significantly higher than backscattered photons at lower TMFPs, and

the reconstruction results of different methods all have significantly higher contrast. However, due to the close coupling of forward-scattered and ballistic photons, time-gating, cross-correlation, and BMM are unable to deal with the artifacts formed by forward-scattered light, and there is blurring in the reconstruction results. With the increasing distance of the object, the forward scattering effect is increasing, while the signal photons from the object are gradually decreasing, the reconstruction quality of time-gating, cross correlation, and BMM decreases significantly, and the object starts to become invisible at 7.360 TMFPs. The proposed method, on the other hand, can effectively deal with both forward-scattered and backward-scattered light during the imaging process, and still maintains a clear reconstruction of the object with increasing TMFPs, and remains effective at 9.568 TMFPs. Since the photon transmission process is a round-trip optical path, the total optical path of traveled photons is approximately 19 TMFPs.
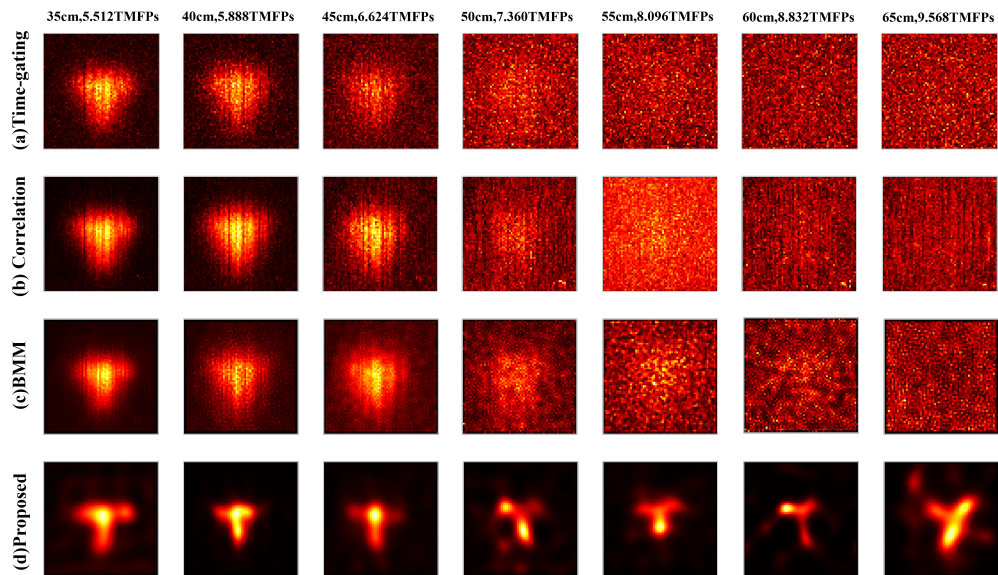

Fig. 6. Object reconstruction results with different TMFPs

To intuitively compare the reconstruction results of different methods under varying TMFPs, we calculated the PSNR and SSIM for all outcomes, as shown in Tables 3 and 4. Due to backward scattering and water absorption, the contrast of the reconstruction results using time-gating, cross-correlation, and BMM methods significantly decreases, with PSNR dropping notably as TMFPs increase. Additionally, forward scattering causes increasing blurring as scattering increases, leading to severe morphological loss in the reconstructions from these methods, which corresponds to a significant decrease in SSIM. In contrast, the proposed method consistently reconstructs the target object clearly and effectively, even as underwater scattering increases. The PSNR and SSIM remain optimal and stable, demonstrating the proposed method's effectiveness.

Table 3. Comparison in PSNR(dB) of Different TMFPs

TMFPs	5.152	5.888	6.624	7.360	8.096	8.832	9.568	Average
Time-gating	10.4405	9.0137	8.0395	5.3151	5.9209	5.7270	4.8991	7.050
Correlation	9.9952	9.6187	8.8203	7.4421	7.4990	6.3146	5.2360	7.8465
BMM	12.2114	12.0835	10.4686	9.9813	8.5790	9.4508	8.5247	10.1856
Proposed	**14.0964**	**13.5433**	**12.5370**	**13.1334**	**12.5761**	**12.9613**	**12.6500**	**13.0710**

Table 4. Comparison in SSIM of Different TMFPs

TMFPs	5.152	5.888	6.624	7.360	8.096	8.832	9.568	Average
Time-gating	0.4819	0.3835	0.2350	0.0773	0.0812	0.0655	0.0205	0.1921
Correlation	0.4478	0.3761	0.2680	0.1477	0.0478	0.0423	0.0371	0.1952
BMM	0.5097	0.4050	0.3052	0.2177	0.1437	0.1350	0.1187	0.2621
Proposed	**0.6321**	**0.5695**	**0.4527**	**0.5792**	**0.5574**	**0.3913**	**0.5137**	**0.5279**

4. Conclusion

In this paper, we present a novel forward-backward-distinctive imaging model to address the limitations of existing TOF-based underwater imaging methods. By modeling the forward-scattered illumination with a point spread function and the backward-scattered field with diffusion equation, our approach effectively captures the anisotropic scattering characteristics of turbid water and comprehensively models the scattering propagation process. The derived underwater boundary migration model establishes a clear mapping between the scene and the measurements, enabling a robust reconstruction algorithm that utilizes TOF information by solving the inverse problem. We verified the effectiveness of the proposed method using a laboratory-simulated turbid water environment and a real imaging system. Experimental results demonstrate that our method significantly outperforms current methods, achieving superior visual quality, PSNR, and SSIM. It successfully reconstructs objects with higher accuracy and greater imaging limits, even at a one-way scattering length of 9.5 TMFPs (19 TMFPs round-trip), confirming the correctness of the model and the effectiveness of the algorithm.

Disclosures. The authors declare no conflicts of interest.

Data availability. Data underlying the results presented in this paper are not publicly available at this time but may be obtained from the authors upon reasonable request.

References

1. Z. Xu and D. K. Yue, "Analytical solution of beam spread function for ocean light radiative transfer," Opt. Express **23**(14), 17966–17978 (2015).
2. Y. Kuga, A. Ishimaru, H.-W. Chang, *et al.*, "Comparisons between the small-angle approximation and the numerical solution for radiative transfer theory," Appl. Opt. **25**(21), 3803–3805 (1986).
3. O. Korotkova, "Light propagation in a turbulent ocean," in *Progress in Optics*, vol. 64 (Elsevier, 2019), pp. 1–43.
4. S. Q. Duntley, "Underwater lighting by submerged lasers and incandescent sources," (1971).
5. P. Drews, E. Nascimento, F. Moraes, *et al.*, "Transmission estimation in underwater single images," in *Proceedings of the IEEE international conference on computer vision workshops*, (2013), pp. 825–830.
6. D. Berman, D. Levy, S. Avidan, *et al.*, "Underwater single image color restoration using haze-lines and a new quantitative dataset," IEEE transactions on pattern analysis and machine intelligence **43**, 2822–2837 (2020).
7. P. Zhuang, J. Wu, F. Porikli, *et al.*, "Underwater image enhancement with hyper-laplacian reflectance priors," IEEE Trans. on Image Process. **31**, 5442–5455 (2022).
8. P. Zhuang, C. Li, and J. Wu, "Bayesian retinex underwater image enhancement," Eng. Appl. Artif. Intell. **101**, 104171 (2021).
9. P. Mariani, I. Quincoces, K. H. Haugholt, *et al.*, "Range-gated imaging system for underwater monitoring in ocean environment," Sustainability **11**(1), 162 (2018).
10. P. Risholm, J. Thorstensen, J. T. Thielemann, *et al.*, "Real-time super-resolved 3d in turbid water using a fast range-gated cmos camera," Appl. Opt. **57**(14), 3927–3937 (2018).
11. F. Caimi and F. Dalgleish, "Performance considerations for continuous-wave and pulsed laser line scan (lls) imaging systems," J. Eur. Opt. Soc.-Rapid Publ. **5**, 10020s (2010).
12. A. Maccarone, A. McCarthy, X. Ren, *et al.*, "Underwater depth imaging using time-correlated single-photon counting," Opt. Express **23**(26), 33911–33926 (2015).
13. A. Maccarone, A. McCarthy, A. Halimi, *et al.*, "Depth imaging in highly scattering underwater environments using time-correlated single-photon counting," in *Emerging Imaging and Sensing Technologies*, vol. 9992 (SPIE, 2016), pp. 154–161.

14. A. Maccarone, G. Acconcia, U. Steinlehner, *et al.*, "Custom-technology single-photon avalanche diode linear detector array for underwater depth imaging," Sensors **21**(14), 4850 (2021).

15. A. Maccarone, F. M. Della Rocca, A. McCarthy, *et al.*, "Three-dimensional imaging of stationary and moving targets in turbid underwater environments using a single-photon detector array," Opt. Express **27**(20), 28437–28456 (2019).

16. F. Heide, L. Xiao, A. Kolb, *et al.*, "Imaging in scattering media using correlation image sensors and sparse convolutional coding," Opt. Express **22**(21), 26338–26350 (2014).

17. H. Lu, Y. Zhang, Y. Li, *et al.*, "Depth map reconstruction for underwater kinect camera using inpainting and local image mode filtering," IEEE Access **5**, 7115–7122 (2017).

18. X. Yin, H. Cheng, K. Yang, *et al.*, "Bayesian reconstruction method for underwater 3d range-gated imaging enhancement," Appl. Opt. **59**(2), 370–379 (2020).

19. A. Halimi, A. Maccarone, R. A. Lamb, *et al.*, "Robust and guided bayesian reconstruction of single-photon 3d lidar data: Application to multispectral and underwater imaging," IEEE Trans. Comput. Imaging **7**, 961–974 (2021).

20. R. Wu, J. Suo, F. Dai, *et al.*, "Scattering robust 3d reconstruction via polarized transient imaging," Opt. Lett. **41**(17), 3948–3951 (2016).

21. R. Wu, A. Jarabo, J. Suo, *et al.*, "Adaptive polarization-difference transient imaging for depth estimation in scattering media," Opt. Lett. **43**(6), 1299–1302 (2018).

22. D. B. Lindell and G. Wetzstein, "Three-dimensional imaging through scattering media based on confocal diffuse tomography," Nat. Commun. **11**(1), 4517 (2020).

23. D. Du, X. Jin, R. Deng, *et al.*, "A boundary migration model for imaging within volumetric scattering media," Nat. Commun. **13**(1), 3234 (2022).

24. D. Du, X. Jin, and R. Deng, "Non-confocal 3d reconstruction in volumetric scattering scenario," IEEE Trans. Comput. Imaging **9**, 732–744 (2023).

25. Y. Chen, M. Xia, W. Li, *et al.*, "Comparison of point spread models for underwater image restoration," Optik **123**(9), 753–757 (2012).

26. W. Hou, D. J. Gray, A. D. Weidemann, *et al.*, "Comparison and validation of point spread models for imaging in natural waters," Opt. Express **16**(13), 9958–9965 (2008).

27. W. H. Wells, "Theory of small angle scattering," in *Optics of the Sea*, vol. 61 (IEEE, 1973).

28. W. Hou, D. Gray, A. Weidemann, *et al.*, "A practical point spread model for ocean waters," in *IV International Conf. Current Problems in Optics of Natural Waters*, (2007), pp. 86–90.

29. D. B. Lindell, G. Wetzstein, and M. O'Toole, "Wave-based non-line-of-sight imaging using fast fk migration," ACM Trans. Graph. **38**(4), 1–13 (2019).